A Projection Algorithm for Satellite Rainfall Detection

NAZARIO D. RAMIREZ-BELTRAN[1], ROBERT J. KULIGOWSKI[2], JOAN M. CASTRO[3], MELVIN J. CARDONA[3] and RAMON VASQUEZ[3].

[1]Department of Industrial Engineering, University of Puerto Rico, P.O. Box 9030, Mayagüez, PR 00681, U.S.A, nazario@ece.uprm.edu

[2]NOAA/NESDIS Center for Satellite Applications and Research (STAR), Camp Springs, MD 20746, U.S.A. Bob.Kuligowski@noaa.gov

[3]Department of Computer and Electrical Engineering, University of Puerto Rico, P.O. Box 9040, Mayagüez, PR 00681, U.S.A, joan.castro@upr.edu, cardonam@gmail.com, reve@ece.uprm.edu

Abstract – A projection algorithm to detect rain cloud pixels in visible and infrared satellite data is introduced in this work. The algorithm is based on the angle formed by two vectors in the n-dimensional space. This algorithm takes advantages of the geometrical projection principle: when two vectors are collinear the radiative variables of clouds used to create the vectors may exhibit similar properties, and when the vectors are orthogonal the radiative variables may have no elements in common. Rain/no rain pixels are identified by using radar rain rate over the studied area. Satellite data from visible and infrared channels are used to create rain and no rain pixel populations. The central tendency of each population is used to generate rain and no rain calibration vectors. A pixel from an independent data set is used to create a third vector, which is projected into the previously calibrated vectors, with the purpose of classifying the third vector in one of the two populations, rain or no rain. Classification is made depending of the magnitude of the projection angle and the probability distribution of the visible and infrared radiation variables. The proposed algorithm was implemented to detect rain clouds over a tropical area with the special purpose of developing an application to improve the Hydro-Estimator, which is an operational and high-resolution rainfall retrieval algorithm that has been applied over the United States since 2002.

Key-words - Vector projection, classification, warm rainy clouds, rainfall detection algorithm, Hooke-Jeeves pattern search.

1. Introduction

The occurrence of rainfall in a given area and during a particular point in time can be considered as a sequence of rain/no rain events. Thus, the rainfall detection process can be viewed as a classification process. The challenge in this work is to infer the presence of rainfall in a pixel by looking the visual reflectance and the brightness temperatures obtained from satellite infrared (IR) channels. This radiative information has been selected because data from a Geostationary Operational Environmental Satellite (GOES) are provided at high spatial and temporal resolution. It is well known that for convective processes the presence of heavy rainfall is associated with cold clouds. However, there are cold clouds

with no rain, and also there are heavy rains from warm clouds. Thus, there is a need for an unbiased classification algorithm that groups a set of rain/no rain pixels with similar radiative properties within a group and rain/no rain pixels with different radiative properties among the groups. Bankert et al. [1] pointed out that there exist different ways of classifying clouds (e.g, by altitude, classical types, physical characteristics, etc). In addition, many classification methods exist and could be applied to achieve the most accurate and most appropriate classification, given the output required from the classifier. Depending upon the user's needs or application, the classifier can be developed through theoretical (explicit physics) or empirical/statistical (implicit physics) methods. Bankert et al. [1] developed two cloud classifiers: one based on physics and the other on statistics, using GOES-11 radiative information. The empirical algorithm used an unsupervised artificial neural network technique. The physical method used the physical properties of clouds to identify the different classes of clouds.

Diner et al. [2] developed a cloud classification by using Multi-angle Imaging Spectro-Radiometer (MISR) data to partition clouds into categories distinguished by parameters such as: cloud elevation, angular signature, and texture or degree-of-brokenness (e.g., stratiform vs. cumuliform). This theoretically-based algorithm is used to retrieve the cloud classification parameters of the MISR Level 2 Top-of-Atmosphere (TOA)/Cloud Product.

A cloud classification scheme was also developed by Col and Mouchot [3] based on the Special Sensor Microwave Imager (SSM/I) measurements in association with the Meteorological Satellite (METEOSAT) classification. Before classifying SSM/I data, an objective technique is applied to enhance spatial resolution of measurements to the resolution of the 37 GHz channel. Different classification algorithms have been performed. The Fuzzy C-Mean algorithm seems to provide the best match with the METEOSAT classification, used as the ground truth.

Although, Bankert et al. [1] Diner et al. [2] and Col and Mouchot [3] developed comprehensive and reliable algorithms for cloud classification, they are not directly applicable to this research effort, since this paper is focused on classifying cloud pixels into raining and non-raining pixels.

Since radar and satellite provide high resolution data, a computationally fast algorithm is required for processing data and performing rain/no rain pixel detection. The algorithm that is proposed here exhibits a high computational skill and is based on the geometric representations of two vectors in an n-dimensional space. The introduced algorithm is especially useful for identifying the rain/no rain pixels in a storm, where no radar is available. Although during the model calibration process radar is required.

The second section of this paper presents the description of the radar and satellite data used by the rainfall detection algorithm (the former only for calibration purposes). The third section presents the description of the proposed projection algorithm for detecting rain/no rain pixels. The fourth section describes a real-world application of the projection algorithm to identify rain/no rain clouds over a tropical basin. The fifth section presents a summary and conclusions of the research work.

2. Data collection

The data of this study are associated with a convective storm, and come from two sources of measurements: radar and satellite. Thus, the studied area is limited by the coverage of the radar. Although the algorithm was designed for Puerto Rico, it is expected that the algorithm can be implemented in any other tropical region.

NEXRAD data over Puerto Rico come from a WSR-88D unit located in Cayey (18.12°N, 66.08°W, 886.63 m elevation). The radar frequency is 2.7 GHz and the maximum horizontal range is 462 km, and the radar scans the entire island every 6

minutes. The study area covers 121x121 radar pixels with a grid size of 0.025^o $(2.6 \times 2.8\,\text{km})$. Level III data for PR are available continuously since 2000 [4], so the Level III data were selected to implement the detection algorithm. The scanning angle for reflectivity data was selected as 0.5 degrees for this research in order to avoid beam overshoot over western PR.

Four bands of the GOES imager are used as input to the rainfall detection algorithm: visible (0.65 μm), near infrared (3.9 μm), water vapor (6.7 μm), and thermal IR (10.7 μm). Two band differences were also calculated: the brightness temperature difference for 3.9μm - 10.7-μm and the difference for 6.7μm - 10.7μm. In order to consider the cloud elevation and wind speed, an indirect measurement of elevation and wind effect (proxy variable) may be captured by computing the differences of two consecutives brightness temperature measurements from the thermal IR channel and two consecutive brightness temperature measurements from the water vapor channel.

Cloud microphysics can be derived by studying the infrared channel. Turk at al. [5] used the GOES 8 and 9 the near infrared channel that sense radiation at 3.9 μm and the shortwave channel at 3.7 μm from the Advanced Very High Resolution Radiometer (AVHRR) instrument aboard the NOAA polar-orbiting satellite systems. In this spectral region, daytime satellite-observed radiances include contributions from both the reflected solar radiation and the emitted thermal emission. In particular, typical stratus and fog clouds exhibit near-infrared emissivities less than unity, which requires special processing to account for the angular dependence of the solar reflection. They showed a side-by-side comparison of time-coincident GOES- and AVHRR-derived near-infrared cloud reflectance is carried out in order to demonstrate the capability of GOES-8 and -9 in both identifying and characterizing the microphysics of stratus and fog clouds during the daytime. They also used satellite data to retrieve cloud drop size distribution and effective radius over the coastal California during the summer of 1996.

During the daytime the visible and IR channels are available; however, during the nighttime only the IR channels provide meaningful data since there is no reflected solar radiation. Albedo was computed using a method presented by Lindsey and Grasso [6]. They developed an algorithm based on the total radiance of channel 2 (3.9 μm), solar irradiance, and the equivalent black body emitted by thermal radiation at 3.9 μm for a cloud at temperature *T*.

GOES data were collected every 15 minutes and comes at approximately $4x4km^2$ spatial resolution. The collected data were organized into 15–minutes intervals; i.e., radar pixels were allocated to the closest satellite pixels in time and space. Table 1 shows the list of studied variables: 7 variables during nighttimes and 9 variables during the daytimes.

Table 1. Algorithm input variables.

No	Variable Name	Variable Description
1	Tb2	Brightness temperature from channel 2
2	Tb3	Brightness temperature from channel 3
3	Tb4	Brightness temperature from channel 4
4	Tb3(t-1)	Difference of two consecutives brightness temperature of channel 3.
5	Tb4(t-1)	Difference of two consecutives brightness temperature of channel 4.
6	Tb24	Difference of Tb2 – Tb4
7	Tb34	Difference of Tb3 – Tb4
8	Vr	Visual reflectance of channel 1
9	Albedo	Albedo of channel 2

3. Projection algorithm

A computationally fast algorithm is proposed to classify rain and no rain pixels. The algorithm starts by organizing the data. Since satellite information is different during the day and night, the data are separated in two groups; data associated to pixels during the daytime and nighttime, respectively. Each data set is also divided

in three parts: data for calibration, for validation and for detection. The calibration data are used for designing the projection vectors, the validation data are for testing the algorithm performance and the detection data are for implementing the algorithm.

The first (calibration) step of the algorithm requires identifying the location of rain/no rain pixels over the study area, and the radar rain rate data are used for this purpose. The identified pixels are used to create the rain and no rain pixel populations. The data set for calibration is used to calculate the central tendency of each population and can be used to create two vectors: the rain and no-rain vectors. The second (application) step of the projection algorithm consists of selecting a pixel (from the validation data) that will be classified as a rain/no rain pixel. Data from this pixel will be used to create a third vector, which will be projected onto the rain and no rain vectors. The magnitude of the projection angles and the probability distribution of radiative variables will be used to classify the pixel. In addition to the previous steps the projection algorithm includes the following subtasks:

2.1 Pixel classification.

The calibration data will be divided into eight groups as shown in Figure 1. Groups 1-4 correspond to no rain pixels and groups 5-8 are associated to rain pixels. Groups 1 and 5 have the coldest pixels with $T < 220K$, where T is the brightness temperature of channel 4 in degrees Kelvin . Groups 2 and 6 have semi-cold pixels with $220K \leq T < 235K$. Groups 3 and 7 exhibit warm pixels with $235K \leq T < 250K$ and the groups 4 and 8 show the very warm pixels, i.e., $T \geq 250K$..

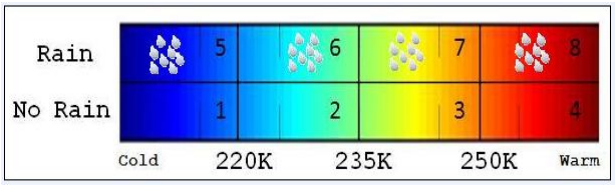

Fig 1 Pixel classification

A calibration pixel is a rain/no rain pixel that is used for model calibration purposes. A calibration rain pixel is located in the center of a square and surrounded by 8 rain pixels as shown in Figure 2, and likewise, a calibration no rain pixel is a no rain pixel located in the center surrounding by 8 no rain pixels (Figure 2). This requirement of the same characteristics in all 9 pixels is intended to reduce potential ambiguity in the training data.

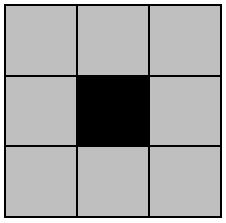

Fig. 2. Rain pixel

2.2 Vector representation of each group

The next step is to compute the average and the standard deviation for the calibration pixels. Although the calibration pixel is the one located in the center of the square, the estimation of the calibration pixel properties is computed by using the 9 pixels that are shown in Figure 2. This is done to reduce noise and derive a more consistent estimator for the pixel that is located in the center of square. Thus, the average and the standard deviation for a calibration pixel are computed as follows:

$$\bar{x}_{jkl} = \frac{1}{n_0}\sum_{i=1}^{n_0} x_{ijkl} \qquad (1)$$

for $j = 1, \dots, n$ $k = 1, \dots, m$ $l = 1, \dots, 8$

$$s_{jkl} = \sqrt{\frac{1}{n_0 - 1}\sum_{i=1}^{n_0}\left(x_{ijkl} - \bar{x}_{jkl}\right)^2} \qquad (2)$$

for $j = 1, \dots, n$ $k = 1, \dots, m$ $l = 1, \dots, 8$

where n_0 is the number of pixels shown in Figure 2 (counted using i), and includes the central pixel and its surrounding pixels; n is the number of pixels in a group (counted using j), and m is the number of

variables in a group (counted using k). The counter l refers to the 8 different pixel classes. The central tendency and the standard deviation for each group are estimated as follows:

$$\bar{\bar{x}}_{kl} = \frac{1}{n}\sum_{j=1}^{n} \bar{x}_{jkl} \qquad (3)$$

for $k = 1, \dots, m$ $l = 1, \dots, 8$

$$\bar{s}_{kl} = \frac{1}{n}\sum_{j=1}^{n} s_{jkl} \qquad (4)$$

for $k = 1, \dots, m$ $l = 1, \dots, 8$

A representative vector for each group is developed by including the central tendency and the standard deviation for each variable in a particular group, as follows:

$$\boldsymbol{c}_l = [\bar{\bar{x}}_{1l}, \ \bar{\bar{x}}_{2l}, \ , \cdots, \ \bar{\bar{x}}_{ml} \ \bar{s}_{1l}, \ \bar{s}_{2l}, \ , \cdots, \ \bar{s}_{ml}] \quad (5)$$

for $l = 1, \dots, 8$

2.3 Vector to be projected

A validation pixel is a pixel that is located in the center of the square as in Figure 2 and its properties are estimated by using its value and the value of the 8 surrounding pixels. This calculation is similar to the validation process. However, in this case there is no rainfall information about the pixels: they could be rain, no rain, or mixed pixels. A validation pixel is extracted to determine to which group of pixels show similar characteristics to the calibrated pixel. The average and standard deviation of the validation pixel (nine pixels) are computed for the radiative variables (Table 1). The averages and the standard deviations are used to create the projection vector, which can be represented as follows:

$$\boldsymbol{p} = [\bar{x}_1, \ \bar{x}_2, \ , \cdots, \ \bar{x}_m, \ s_1, \ s_2, \ , \cdots, \ s_m] \quad (6)$$

where $\bar{x}_k$ and s_k are the average and the standard deviation of the validation pixel (i.e., 9 pixels) for $k = 1, \dots, m$.

2.4 Compute projection angle

The projection angle is the angle between the central vector ($\boldsymbol{c}_l$) and the projection vector ($\boldsymbol{p}$). The definition of the inner product is used to calculate the angle between vectors in the n-dimensional space and can be expressed as follows [7]:

$$\theta_l = cos^{-1}\left(\frac{\boldsymbol{p} \cdot \boldsymbol{c}_l}{\|\boldsymbol{p}\|\|\boldsymbol{c}_l\|}\right) \qquad (7)$$

where $\boldsymbol{p} \cdot \boldsymbol{c}_l$ is the inner product between the $\boldsymbol{p}$ and $\boldsymbol{c}_l$ vectors**;** $\|\boldsymbol{p}\|$ is the module of the vector $\boldsymbol{p}$ and $\|\boldsymbol{c}_l\|$ is the module of the vector $\boldsymbol{c}_l$**.**

2.5 Compute confidence interval

Confidence intervals are computed for the mean and the standard deviation of each variable in each group. The confidence intervals are developed based on the populations of means and standard deviations which were computed using equations (1) and (2). The confidence intervals were estimated by computing the $\alpha_{L,kl}$, $\alpha_{U,kl}$, $\delta_{L,kl}$ and $\delta_{U,kl}$ percentiles for $k = 1, \dots, m$ and $l = 1, \dots, 8$; where $\alpha_{L,kl}$ and $\alpha_{U,kl}$ are the lower and upper limits for the mean and $\delta_{L,kl}$ and $\delta_{U,kl}$ are the lower and upper limits for the standard deviation of calibration data. The confidence intervals are computed in a way to maximize the performance of the algorithm. The Hooke-Jeeves pattern search method [8] is used to estimate the confidence intervals for each variable in such a way that the index of performance is minimized, which is defined as follows:

$$index = \frac{\overline{FAR} - \overline{POD} - \overline{HR} + 2}{3} \qquad (8)$$

Thus minimizing the index implies to minimize the average false alarm rate ($\overline{FAR}$), and maximize the average of probability of detection ($\overline{POD}$) and maximizing the average hit rate ($\overline{HR}$).

2.6 Pixel classification

The group L that is associated with the minimum projection angle is identified, where L is computed as follows:

$$L = min\{\theta_l\}, \quad l = 1, \dots, 8 \qquad (9)$$

A validation pixel is classified in the L^{th} group if the majority of the variables satisfy the confidence interval conditions. The k^{th} variable satisfied the confidence interval conditions if the average ($\bar{x}_k$) and the standard deviation (s_k) of a validation pixel fall inside of the corresponding confidence intervals. If the confidence interval conditions are not satisfied, the projection angle that falls in second ranking position (*M*) is selected. The interval confidence conditions are tested again for the group associated with the second angle and if the confidence interval conditions are satisfied, the validation pixel is assigned to the M^{th} group; otherwise, the majority voting criterion is used. The majority voting consists of classifying a pixel as rainy if the three smallest projection angles are associated with rainy groups; otherwise, the validation pixel is assigned to a no-rain pixel.

4. Preliminary results

During October 27-29, 2007 an African wave that becomes the precursor of the hurricane Noel passed over Puerto Rico. This paper presents preliminary results associated during the first day of the storm. Table 2 shows the central tendency and the standard deviation for each variable and for each group during the daytimes. These results were obtained using equations (3) and (4).

Table 2. Central tendency for each group

Variable	Group							
	No rain				Rain			
	cold	Semi cold	warm	Very warm	cold	Semi cold	warm	Very warm
	1	2	3	4	5	6	7	8
Tb2	245	249	260	276	242	248	252	260
Tb3	214	223	231	241	213	224	231	239
Tb4	216	229	243	265	215	228	240	256
Tb3(t-1)	-1.0	-0.3	-0.3	0.4	-1.0	-0.8	0.4	0.5
Tb4(t-1)	-1.3	-1.6	-2.0	1.3	-0.1	-1.0	1.1	2.1
Tb24	28	21	17	11	28	20	11	4
Tb34	2	6	12	24	1	4	9	17
Vr	6.34	7.04	11.41	20.61	4.38	4.76	4.50	3.76
Albedo	0.13	0.11	0.09	0.06	0.14	0.14	0.12	0.12

Table 3. Standard deviation for each group

Variable	Group							
	No rain				Rain			
	cold	Semi cold	warm	Very warm	cold	Semi cold	warm	Very warm
	1	2	3	4	5	6	7	8
Tb2	1.95	2.75	3.95	3.70	1.84	1.94	2.77	2.85
Tb3	1.50	1.69	1.76	0.91	1.63	1.87	2.01	1.37
Tb4	2.01	2.93	4.20	3.61	1.82	2.72	3.87	3.32
Tb3(t-1)	1.70	2.23	2.25	1.20	2.94	2.73	2.79	2.60
Tb4(t-1)	2.19	3.83	5.08	4.46	2.00	3.23	4.15	3.67
Tb24	1.77	2.11	2.42	2.24	2.39	2.39	2.61	1.90
Tb34	0.94	1.52	2.72	2.99	0.69	1.18	2.13	2.19
Vr	0.89	1.48	2.76	5.11	0.49	0.61	0.90	1.35
Albedo	0.01	0.01	0.01	0.02	0.01	0.01	0.02	0.03

The performance of the algorithm is measured by the discrete validation scores: probability of detection (POD), false alarm rate (FAR), hit rate (HR) and bias ratio (BR). The pixels detected by NEXRAD are considered as the "ground truth" values and the pixels detected by the HE and projection algorithm (PA) are considered as the estimated rain/ no rain pixels. Average validation scores are presented on Table 4 and the individual validation score for every 15 minutes interval are given in Figure 3. To perform comparison of PA with an existing algorithm Table 4 and Figure 3 show validation results associated to Hydro-Estimator (HE) [9, 10, 11, 12]. The HE has been the operational satellite rainfall algorithm of the National Environmental Satellite, Data, and Information Service (NESDIS) since 2002 and produces rainfall estimates at the full

spatial and temporal resolution of GOES over the continental area of United States and surrounding regions, including PR; real-time estimates are also produced on an experimental basis for the rest of the globe. The individual validation scores presented in Figures 3 and 4 show that the HE during the daytime exhibits a strong POD, but poor performances on HR, and FAR. These results are also confirmed in Table 4. This table shows that on the average the performance of the HE and PA are very similar during the nighttime; however, during the daytimes the PA shows better results than the HE in all validation scores except for probability of detection.

Table 4. Validation results for rain / no rain classification during the October 27, 2007 case.

	Daytime Results				Nighttime Results			
	POD	FAR	HR	BR	POD	FAR	HR	BR
Hydro-Estimator	0.97	0.71	0.35	3.56	0.77	0.59	0.73	1.90
Projection algorithm	0.65	0.59	0.66	1.61	0.81	0.58	0.73	1.96

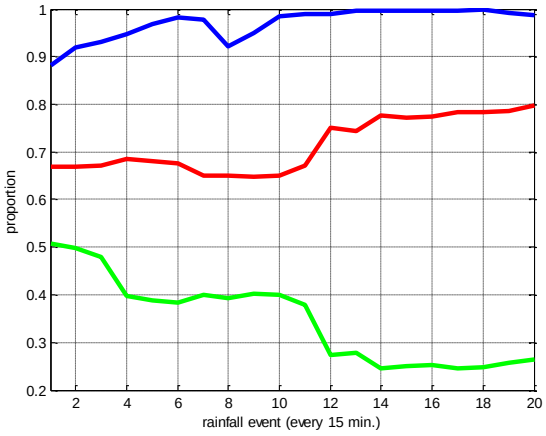

Fig. 3. Validation scores for the Hydro-Estimator. POD in blue, HR in green and FAR in red (daytime, October 27, 2009)

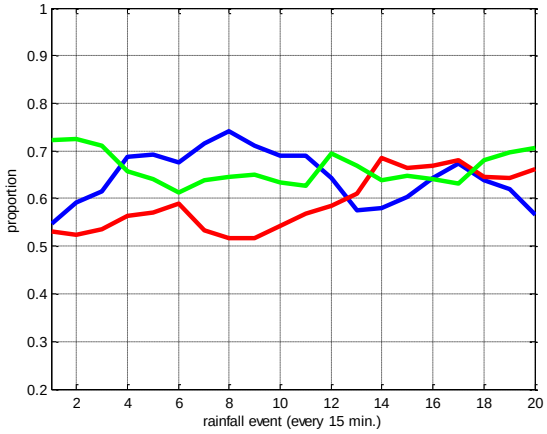

Fig. 4. Validation score for the Projection Algorithm (daytime, October 27, 2009)

Figures 5 and 6 show the rain and no rain pixels detected during 15 minutes (17:45 UTC, October 27, 2007) interval by NEXRAD and HE, respectively. The pixels shown in these figures are limited to the area covered by NEXRAD. The blue area represents no rain pixels and red area represents rain pixels. These figures imply that the HE exhibits a significant overestimation of rainy pixels, consistent with the bias ratio of 3.56 in Table 4.

The PA classifies the pixels into 8 categories at 15-minute intervals (October 27, 17:45 UTC) and the results are shown in Figure 7. This figure shows few dark blue pixels inside of the circle indicate the possible presence of very cold pixels with no rain. Most of these pixels coincide with no rain as shown by radar in Figure 5; however, a few pixels under this group do not meet the confidence interval criterion and they are assigned to cold rain pixels, and the final results of rain/no rain classification are given in Figure 8. Light blue and green colors indicate no rain pixels, and most of these pixels are in agreement with actual no rain pixels detected by the radar (Figure 5). The yellow pixels shown in Figure 7 indicate the presence of very cold clouds with rain pixels and some of these pixels are in agreement with radar rainfall detection, and some pixels represent false alarms. The orange color indicates semi-cold rain pixels and some of these

pixels are also in agreement with radar detection; however, some of these pixels are false alarms. The red color indicates warm rain pixels and the dark red color indicates very warm rain pixels. Most of these red pixels are changed to no rain pixels since they do not meet the confidence interval criterion.

These preliminary results show that during the nighttime the PA provides similar results to the HE. However, during the daytime the PA outperforms the HE, and these results may occur because of the inclusion of visual reflectance and albedo from channel 2. It has been shown that the reflection function at a water (or ice) absorbing channel in the near-infrared is primarily a function of cloud particle size [13]. The reflection function represents the albedo of the medium that would be obtained from a directional reflectance measurement.

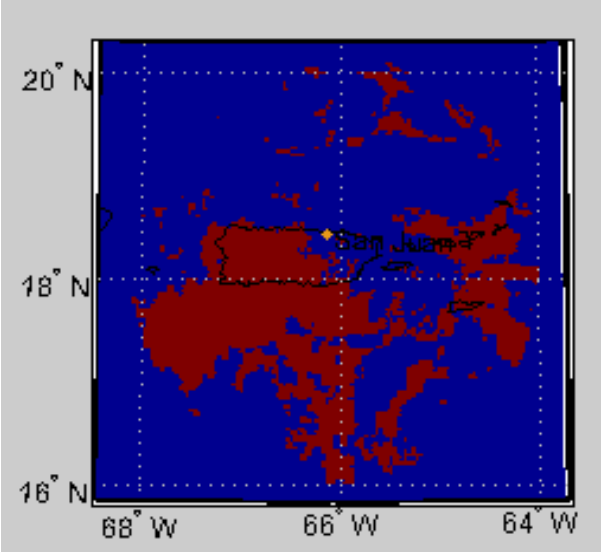

Fig 5. Detected rain/no rain pixel by NEXRAD ("ground truth" of rainfall events) (17:45 UTC, October 27, 2007)

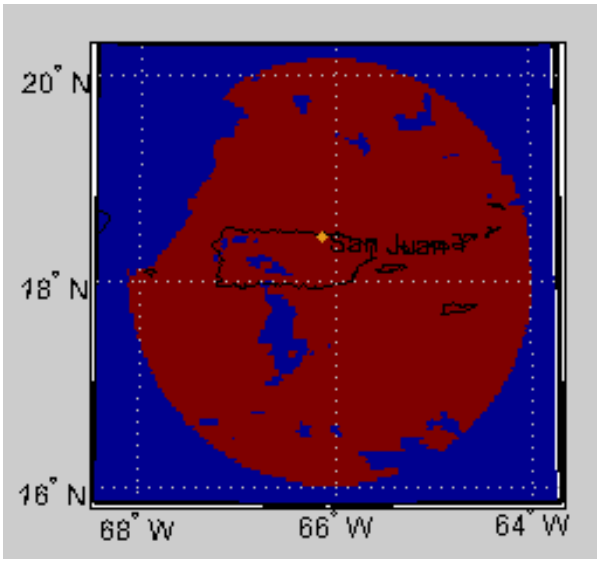

Fig. 6. Estimated rain/no rain pixels by the Hydro-Estimator. (17:45 UTC, October 27, 2007).

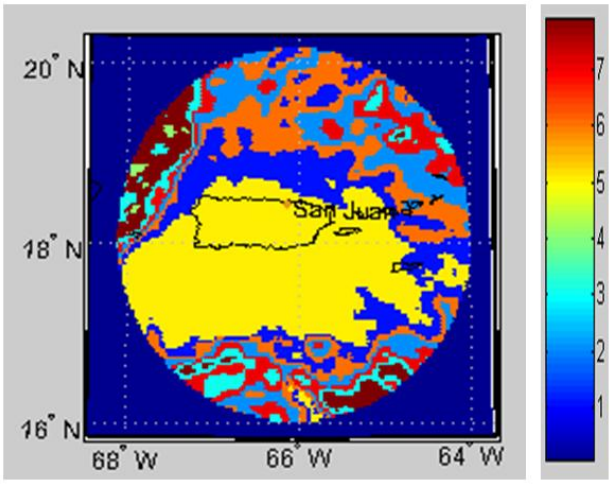

Fig. 7. Classification of pixels into eight different groups. (17:45 UTC, October 27, 2007).

The PA has been based only on radiative cloud properties, i.e., there may be some detection improvements after including atmospheric variables obtained from a numerical weather prediction model. The inclusion of satellite microwave information may also improve the detection skill of the PA.

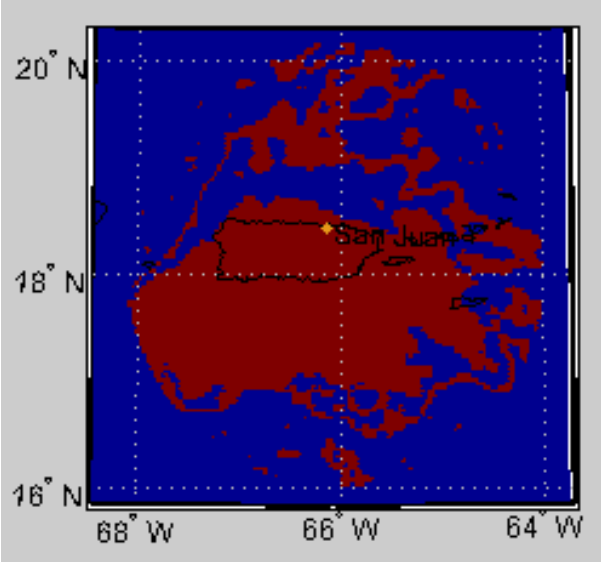

Fig. 8. Estimated rain/no rain pixels by the projection algorithm. (17:45 UTC, October 27, 2007).

5. Conclusions

The PA is a computationally fast algorithm to determine the rain/no rain pixel in tropical convective storms. The PA is based on the geometric representation of a set of information. The PA organizes the radiative properties of clouds into eight different groups, and each group is represented by the central tendency of the radiative properties of the included pixels. An unknown pixel is classified into one of the eight groups. The classification is accomplished by using the radiative properties of an unknown pixel. The radiative properties of the central and surrounding 8 pixels are used to generate a vector, which is projected into the central vectors, and the magnitude of the three smallest angles and the confidences intervals of the involved radiative variables are used to determine the group that should be assigned, and finally the pixel is classified as a rain / no rain pixel.

More experimental work is required to establish a conclusive statement about the advantages of the PA. However, preliminary results indicate that the PA provides a potential improvement of the HE especially during the daytimes. An ongoing project is exploring the possibility of applying this improvement to the operational version of the HE.

6. Acknowledgements.

This research has been supported by the NOAA-CREST grant number NA06OAR4810162, the NSF-ERC-CASA with a grant Number 0313747, the NOAA-NWS grant number NA08NWS4680043, and also by the University of Puerto Rico at Mayagüez. The authors appreciate and recognize the funding support from these institutions.

References

[1] Bankert, R.L., C. Mitrescu, S. D. Miller, and Robert H. Wade, Comparison of GOES Cloud Classification Algorithms Employing Explicit and Implicit Physics. Proceedings of the 5th *GOES Users' Conf.*, *Amer. Meteor. Soc.*, New Orleans, LA, January, 2008.

[2] Diner, D.J., R. Davies, L. D. Girolamo, J.P. Muller, D. Wenkert, J. Zong, C. Moroney, S. R. Paradise, MISR level 2 Cloud Detection and Classification Algorithm Theoretical Basis. *Jet Propulsion Laboratory, California Institute of Technology*, 1999.

[3] Col, B., and M. C. Mouchot, (1995). Cloud Classification using Passive Microwave Satellite Measurements from the SSMn Radiometer. IEEE , pp 1889-1891.

[4] NCDC, National Climatic Data Center: Data Documentation for DSI – 7000 – *NEXRAD Level III. NCDC*, Asheville, NC, 2005

[5] Turk, J., J.T.Vivekanandan, T. Lee, P. Durkee, and K. Nielsen, (1998). Derivation and Applications of Near-Infrared Cloud Reflectances from GOES-8 and GOES-9. J. Applied Meteor., Vol., 37, pp 817-831.

[6] Lindsey, D., and Grasso, L., An effectives radius for thick ice clouds using GOES. *J. Applied Meteor. and Climat.*, Vol.47, 2008, pp. 1222-1231.

[7] Strang, G., Linear Algebra and its Applications, Academic Press, New York, 1976, pp. 418.

[8] Reklaitis, G.V., A. Ravindran, and K.M. Ragsdell, (1983) *Engineering Optimization: Methods and Applications*. John Wiley, New York, p 684.

[9] Scofield, R.A., and R.J. Kuligowski, 2003: Status and outlook of operational satellite precipitation algorithms for extreme-precipitation events. Wea. *Forecasting*, Vol.18, pp. 1037-1051.

[10]. Harmsen, E. W., S. E. Gomez Mesa, E. Cabassa, N. D. Ramírez-Beltran, S. Cruz Pol, R. J. Kuligowski And R. Vasquez, 2008. Satellite sub-pixel rainfall variability. *International Journal of Systems Applications, Engineering and Development*, Vol.2, No.3, 2008, pp. 91-100.

[11]. Ramírez-Beltran, N.D, Kuligowski, R.J., Harmsen, E., Castro, J.M., Cruz-Pol, S., Cardona-Soto, M., Rainfall Estimation from Convective Storms Using the Hydro-Estimator and NEXRAD. *WSEAS Transaction on Systems*. Vol.7, No.10, 2008, pp. 1016-1027.

[12] Ramírez-Beltran, N.D, Kuligowski, R.J., Harmsen, E., Castro, J.M., Cruz-Pol, S., Cardona-Soto, M., Validation and Strategies to Improve the Hydro-Estimator and NEXRAD over Puerto Rico. Proceedings of the 12th *WSEAS International Conference on Systems*. Heraklion, Crete, Greece, July 22-24, 2008, pp. 799-806.

[13] Nakajima, T., and M.D. King, 1990. Determination of the Optical Thickness and Effective Particles Radius of Clouds from Reflected Solar Radiation Measurements. Part I: Theory. *J. Atmospheric Sciences*, Vol. 47, No.15, 1990 pp. 1878-1893.